Design and Analysis of Two Doubly Salient Permanent Magnet Machines

Kaikai Guo, Chen Liu, Youguang Guo and Cong Li

***Abstract*—In order to improve the torque density of doubly salient permanent magnet (PM) machine (DSPMM), two different DSPMMs (topologies I and II) with NdFeB PM materials embedded in the stator yoke are presented, and the working magnetic circuits of both topologies contain the main magnetic circuit and auxiliary magnetic circuit through the magnetic barrier beside the PMs, which can improve the air gap flux density and the torque density effectively. The optimization designs of two DSPMMs are analyzed by establishing the equivalent magnetic circuit (EMC) models at no load and load conditions. Another two traditional DSPMMs (topologies III and IV) are taken as the comparison objects, and the best optimal structure parameters of the four topologies are decided by genetic algorithm. A prototype of topology II is manufactured, and the electromagnetic performances of the four DSPMMs are revealed. It is observed that the electromagnetic performances of topology II analyzed by EMC method are in agreement with the results analyzed by finite element method and test results, and the torque of topology II is larger by 148.1%, 27.72% and 245.5% than that of topology I, III and IV, respectively.**

***Index Terms*—Doubly salient permanent magnet machine, equivalent magnetic circuit, finite element method, genetic algorithm.**

I. Introduction

THE doubly salient (DS) permanent magnet (PM) machine (DSPMM) has high torque density and reliability, and many topologies and methods have been presented. A DS hybrid excited motor with fault tolerance capability in the flux weakening region was presented with different combinations of stator and rotor pole numbers [1]. The principles of the least reluctance and the air gap field modulation (AGFM) theory were used to examine the working mechanism of a DSPMM with π-shaped stator core [2]. The nonlinear model of switched reluctance motor (SRM) was proposed based on the least square support vector regression [3]. The electromagnetic characteristics of DSPMM were studied by establishing the equivalent magnetic circuit (EMC) models based on the general AGFM theory [4]. In order to attain the optimal performance of SRM drive system, a multi-objective high-dimensional system level optimization approach was introduced, and the optimal solution was obtained and verified by the finite element method (FEM) [5]. A real time EMC model was developed to effectively simulate the performance of machine [6]. A multi-objective and multi-physics design optimization approach of SRM was investigated to reduce coil temperature and torque ripple comprehensively considering thermal and electromagnetic properties [7].

In this paper, two DSPMMs with PMs embedded in the stator yoke are proposed, the irreversible demagnetization is analyzed to determine the best combination of PM arrangement. The main structural dimensions of DSPMM are optimized based on EMC method and the genetic algorithm (GA). The electromagnetic characteristics of four DSPMMs are analyzed.

II. Topology and Operation Principle

Fig. 1 shows the two topologies of DSPMM. Fig. 2 describes the no-load flux lines and magnetic vector distribution of the two topologies. The circumferentially magnetized PMs with opposite magnetization directions are embedded in the stator yoke of topology I, which are parallel to the sides of the stator teeth and can generate the flux-concentrating effect. The strip and arc magnetic barriers are located at the ends of the PM, respectively. The magnetization directions of PMs corresponding to the adjacent stators are opposite. A combined U-shaped arranged PM is embedded in the stator yoke of topology II. The auxiliary flux circuit (AFC), the main flux circuit (MFC) and the flux leakage circuit (FLC) are marked in Fig. 2. The AFC is established by the adjacent PMs beside the same stator pole, which flows through the strip magnetic barrier and the stator yoke. The auxiliary flux can effectively improve the air gap flux density (AGFD) and torque density.

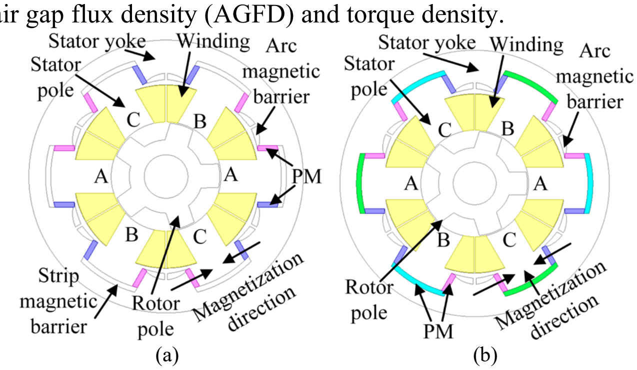

Fig. 1. Topologies of DSPMM. (a) Topology I. (b) Topology II.

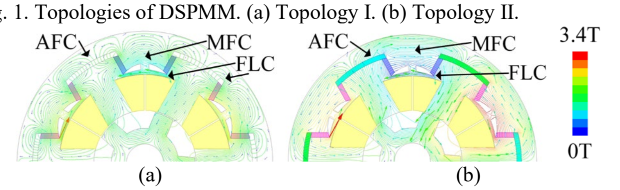

Fig. 2. No-load flux lines and magnetic vector distribution of two DSPMMs. (a) Topology I. (b) Topology II.

Fig. 3 illustrates the structure parameters of the two DSPMMs. R_{so}, R_{si}, R_{ro} and R_{ri} are the outer and inner radii of

This work was supported by the Major Project of School Scientific Research Foundation of Anhui Province under Grant 2022AH040110, the National Natural Science Foundation of China under Grant 51905003, and Natural Science Foundation of Anhui Province under Grant 1908085QE207. (Corresponding author: Kaikai Guo.)

Kaikai Guo, Chen Liu and Cong Li are with the School of Electrical and Information Engineering, Anhui University of Science and Technology, Huainan 232001, China (e-mail: guokai0072000@gmail.com).

Youguang Guo is with the School of Electrical and Data Engineering, University of Technology Sydney, NSW 2007, Australia (e-mail: youguang.guo-1@uts.edu.au).

the stator and rotor, respectively. R_{sy1} and R_{sy2} are the inner radii of stator yoke and the strip magnetic barrier, respectively. R_{rr} is the outer radius of the rotor yoke. W_{rp} and W_{sp} are the widths of rotor and stator poles, respectively. W_{pm1} and W_{pm2} are the thickness of the PMs and strip magnetic barrier of topology I, respectively. W_{sm} is the distance between the adjacent PMs beside the same stator pole. W_{b1} and H_{b1} are the width and height of the flux bridge between the arc magnetic barriers, respectively. H_{L1} and H_{L2} are the widths of the flux bridges below the arc magnetic barrier, respectively.

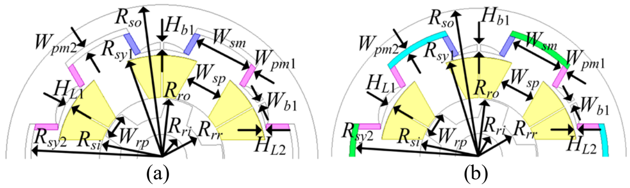

Fig. 3. Structure parameters of two DSPMMs. (a) Topology I. (b) Topology II.

The PM material used for DSPMM is N38SH. The PMs will be demagnetized when the flux density of PM is lower than that of the knee point. As can be seen in Fig. 4, the irreversible demagnetization area below 0.25T in the third arrangement is the smallest when the operating temperature of the machine is 120 ℃. Fig. 5 shows the design flow chart.

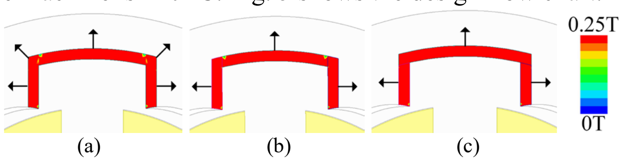

Fig. 4. The demagnetization analysis of PM arrangements at 120°C. (a) The first. (b) The second. (c) The third.

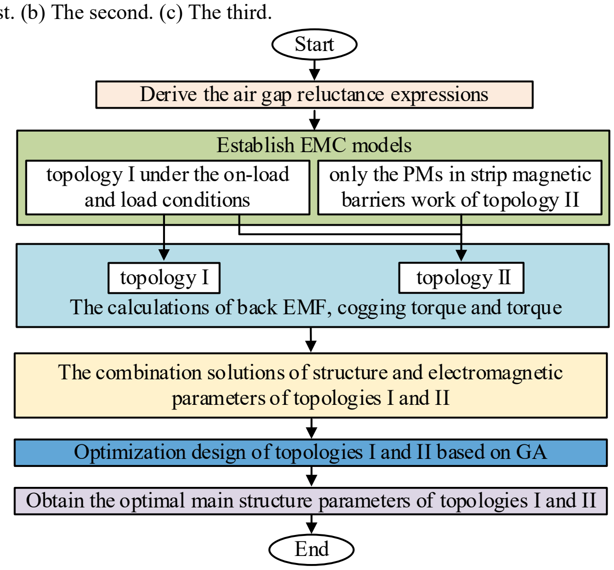

Fig. 5. Design flow chart.

III. Optimization Design

A. Analysis of EMC Model

Fig. 6 describes the relative position of stator pole and rotor pole. θ is the angle between the center lines of stator and rotor poles, and $\theta_3<\theta<\theta_4$. θ_3 and θ_4 are defined as the critical point of air gap region [8], and $\theta_3=90^{\circ}(\tau_r-\tau_s)/\pi$ and $\theta_4=90^{\circ}(\beta_s+\beta_r)/\pi$. τ_s, β_s, τ_r and β_r are the pole pitches and radians of the stator and rotor poles, respectively. According to Fig. 6 (a), the air gap region is divided into three segments, namely $w_1=(\tau_s-\beta_s)R_{si}/2$, $w_2=\pi(\theta_4-\theta)R_{si}/180^{\circ}$ and $w_3=(\tau_r-\beta_r)R_{si}/2$. According to Fig. 6 (b), the air gap reluctance expressions of four segments are

$$R_{g1}(\theta)=\begin{cases}1/[\mu_0 L_a d_1/(g+h_s)],\ 0<d_1<(w_1-s_2)\\ 1/[\mu_0 L_a(w_1-s_2)/(g+h_s)\\ +\int_{w_1-d_1}^{s_2}\mu_0 L_a/(g+\beta_2 x)dx],\ d_1\geqslant(w_1-s_2)\end{cases}\tag{1}$$

$$R_{g2}(\theta)=\begin{cases}1/[\mu_0 L_a(w_1-d_1-s_2)/(g+h_s)\\ +\int_{w_1-2d_1}^{s_2}\mu_0 L_a/(g+\beta_2 x)dx],\ 0<d_1\leqslant(w_1-s_2)\\ 1/[\int_{w_1-2d_1}^{w_1-d_1}\mu_0 L_a/(g+\beta_2 x)dx],\ (w_1-s_2)<d_1\leqslant w_1/2\\ 1/[\int_{0}^{w_1-d_1}\mu_0 L_a/(g+\beta_2 x)dx+\mu_0 L_a(2d_1-w_1)/g],\\ w_1<2d_1\leqslant w_1+w_2\\ 1/[\int_{0}^{w_1-d_1}\mu_0 L_a/(g+\beta_2 x)dx+\mu_0 L_a w_2/g\\ +\int_{0}^{2d_1-w_1-w_2}\mu_0 L_a/(g+\beta_1 x)dx],\ 2d_1>w_1+w_2\end{cases}\tag{2}$$

$$R_{g3}(\theta)=\begin{cases}1/[\int_{0}^{w_1-2d_1}\mu_0 L_a/(g+\beta_2 x)dx+\mu_0 L_a w_2/g\\ +\int_{0}^{3d_1-w_1-w_2}\mu_0 L_a/(g+\beta_1 x)]dx,\\ 2d_1<w_1<3d_1\ \ and\ \ (w_1+w_2)<3d_1\\ 1/[\mu_0 L_a(w_1+w_2-2d_1)/g\\ +\int_{0}^{3d_1-w_1-w_2}\mu_0 L_a/(g+\beta_1 x)dx],\ w_1<2d_1\leqslant w_1+w_2\\ 1/[\int_{2d_1-w_1-w_2}^{3d_1-w_1-w_2}\mu_0 L_a/(g+\beta_1 x)dx],\ 2d_1>w_1+w_2\end{cases}\tag{3}$$

$$R_{g4}(\theta)=\begin{cases}1/[\int_{w_3-d_1}^{w_3}\mu_0 L_a/(g+\beta_1 x)dx],\ s_1\geqslant w_3\\ 1/[\mu_0 L_a(w_3-s_1)/(g+h_r)\\ +\int_{w_3-d_1}^{s_1}\mu_0 L_a/(g+\beta_1 x)dx],\ s_1<w_3\end{cases}\tag{4}$$

where $d_1=(w_1+w_2+w_3)/4$, $\beta_1=(\pi-\beta_r)/2$, $\beta_2=(\pi-\beta_s)/2$, $s_1=h_r/\tan\beta_1$ and $s_2=h_s/\tan\beta_2$. h_r and h_s are the height of the rotor and stator poles, respectively. g is the air gap length. μ_0 is the vacuum permeability. L_a is the effective axial stack length of the DSPMM.

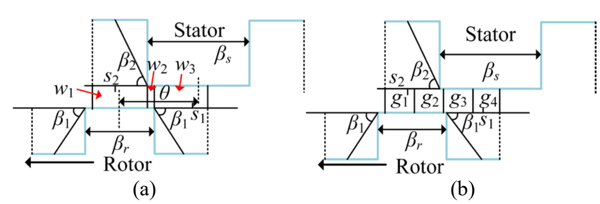

Fig. 6. The relative position of stator pole and rotor pole. (a) Three segments. (b) Four segments.

In order to reduce the complexity of the analysis, a pair of stator poles are selected as the analysis objective. Assume that the permeability of the silicon steel sheets approaches infinity. According to Fig. 2 (a), the no-load and armature magnetic field EMC models of topology I are presented in Fig. 7. Fig. 8

illustrates the simplified main flux no-load and armature magnetic field EMC models of topology I.

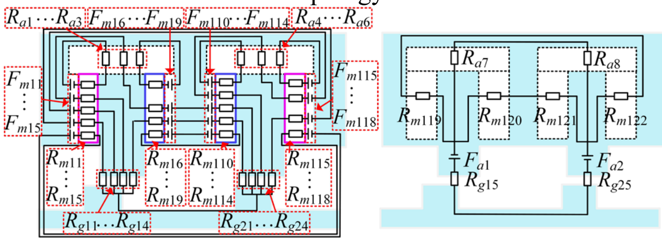

(a) (b)

Fig. 7. No-load and armature magnetic field EMC models of topology I. (a) At no-load condition. (b) Armature magnetic circuit.

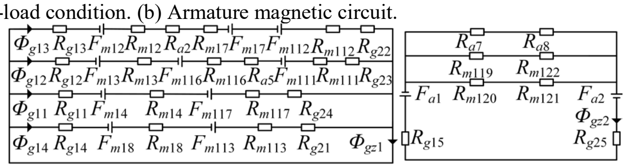

(a) (b)

Fig. 8. The simplified EMC models of topology I. (a) At no-load condition. (b) Armature magnetic circuit.

The expressions of the magnetomotive force (MMF) and the reluctance of the ith PM segment of topology I are

$$F_{m1i}=F_{m1}=H_c W_{pm1}=B_r W_{pm1}/\mu_0\mu_m \tag{5}$$

$$R_{m1i}=W_{pm1}/(\mu_0\mu_m h_{m1i} L_a) \tag{6}$$

where μ_{m}, H_c and B_r are the relative permeability, coercivity and the remanence of PM, respectively. μ_m is taken as1 here. h_{m1i} is the height of the ith PM segment of topology I, and the Fourier expression of h_{m1i} is

$$h_{m1i}(\theta)=\begin{cases} c_i+\sum_{n=1}^{3}[a_{ni}\cos(n\theta\omega_i)+b_{ni}\sin(n\theta\omega_i)], i=1,\cdots,18 \\ R_{sy2}-R_{sy1}-H_{L2}, i=19,\cdots,26 \end{cases} \tag{7}$$

where ω_i, a_{ni}, b_{ni} and c_i are the coefficients of the Fourier expression of h_{m1i}. $h_{m12}(\theta)=h_{m17}(\theta)=h_{m112}(\theta+12°)=h_{m116}(\theta+12°)$, $h_{m15}(\theta)=h_{m118}(\theta)=h_{m19}(\theta+12°)=h_{m114}(\theta+12°)$, $h_{m18}(\theta)=h_{m117}(\theta+12°)$, $h_{m16}(\theta)=h_{m115}(\theta+12°)$ and $h_{m11}(\theta)=h_{m110}(\theta+12°)$.

The expression of the air gap reluctance of the jth segment in the strip magnetic barriers of topology I is

$$R_{aj}=W_{pm2}/(\mu_0 L_a W_{aj}) \tag{8}$$

where W_{aj} is the width of the jth segment in the strip magnetic barriers, and the Fourier expression is

$$W_{aj}(\theta)=\begin{cases} f_j+\sum_{n=1}^{2}[p_{nj}\cos(n\theta u_j)+q_{nj}\sin(n\theta u_j)],\ j=1,\cdots,6 \\ 2W_{pm1}+W_{sm},\ j=7,8 \end{cases} \tag{9}$$

where u_j, f_j, p_{nj} and q_{nj} are the coefficients of the Fourier function of W_{aj}. $W_{aj}(\theta)=W_{a(j+3)}(\theta+12°)$, j=1, 2 and 3.

According to Fig. 7(a), the expressions of the main flux circuits of topology I are

$$\begin{cases} \Phi_{g11}=2F_{m1}/(R_{g11}+R_{m14}+R_{m117}+R_{g24}) \\ \Phi_{g12}=3F_{m1}/(R_{g12}+R_{m13}+R_{m116}+R_{a5}+R_{m111}+R_{g23}) \\ \Phi_{g13}=3F_{m1}/(R_{g13}+R_{m12}+R_{a2}+R_{m17}+R_{m112}+R_{g22}) \\ \Phi_{g14}=2F_{m1}/(R_{g14}+R_{m18}+R_{m113}+R_{g21}) \end{cases} \tag{10}$$

where R_{g11}-R_{g14} and R_{g21}-R_{g24} are the four reluctances of the air gap a_{g1} and a_{g2}, respectively, and they can be obtained by (1)-(4). Φ_{l11}-Φ_{l16} are the flux leakages, $\Phi_{l11}=F_{m1}/(R_{a1}+R_{m11})$, $\Phi_{l12}=F_{m1}/(R_{a3}+R_{m16})$, $\Phi_{l13}=F_{m1}/(R_{a4}+R_{m110})$, $\Phi_{l14}=F_{m1}/(R_{a6}+R_{m115})$, $\Phi_{l15}=2F_{m1}/(R_{m15}+R_{m118})$, and $\Phi_{l16}=2F_{m1}/(R_{m19}+R_{m114})$.

The main air gap flux of topology I at the no-load condition is

$$\Phi_{gz1}=\Phi_{g11}+\Phi_{g12}+\Phi_{g13}+\Phi_{g14} \tag{11}$$

According to Fig. 8(b), the air gap flux of topology I generated by armature magnetic circuit is

$$\Phi_{gz2}=-(F_{a1}+F_{a2})/(R_{g15}+R_{g25}+R_{sag}) \tag{12}$$

where F_{a1} and F_{a2} are the armature MMFs of stator poles 1 and 2, respectively. $F_a=N_c i_{arm}$. The armature current $i_{arm}=I_p\sin(N_r\omega t+\theta_0+\theta_p)$. N_c and N_r are the numbers of turns and rotor poles, respectively. I_p, θ_0, ω and θ_p are the peak value, initial angle, angular velocity and phase of the current, respectively. R_{g15} and R_{g25} are reluctances of the air gap a_{g1} and a_{g2}, respectively. The total air gap reluctance in the stator yoke is

$$R_{sag}=(R_{a7}+R_{a8})//(R_{m119}+R_{m122})//(R_{m120}+R_{m121}) \tag{13}$$

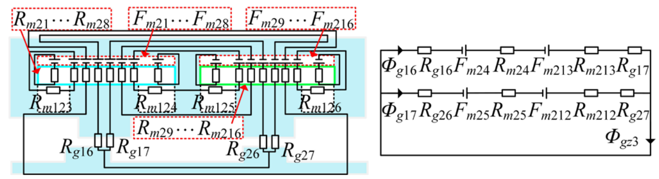

(a) (b)

Fig. 9. Simplified EMC model when only the PMs in strip magnetic barriers work of topology II. (a) EMC model. (b) EMC model of main flux.

Fig. 9 shows the simplified EMC when only the PMs in strip magnetic barriers work of topology II. R_{g16}, R_{g17}, R_{g26} and R_{g27} are respectively the reluctances of the air gap a_{g1} and a_{g2} when the air gap is evenly divided into two parts. F_{m2k} and R_{m2k} are the MMF and the reluctance of the kth PM segment, respectively. W_{m2k} is the width of the kth PM segment in Fig. 9, and the Fourier expression of W_{m2k} is

$$W_{m2k}(\theta)=x_k+\sum_{n=1}^{3}[y_{nk}\cos(n\theta v_k)+z_{nk}\sin(n\theta v_k)], k=1,\cdots,16 \tag{14}$$

where v_k, x_k, y_{nk} and z_{nk} are the coefficients of the Fourier expression of W_{m2k}. $W_{m22}(\theta)=W_{m27}(\theta)$, $W_{m23}(\theta)=W_{m26}(\theta)$, $W_{m210}(\theta)=W_{m215}(\theta)$, $W_{m24}(\theta)=W_{m212}(\theta+12°)$, $W_{m211}(\theta)=W_{m214}(\theta)$ and $W_{m25}(\theta)=W_{m213}(\theta+12°)$.

According to Fig. 8, the expressions of the main flux circuits are

$$\begin{cases} \Phi_{g16}=2F_{m2}/(R_{g16}+R_{m24}+R_{m213}+R_{g17}) \\ \Phi_{g17}=2F_{m2}/(R_{g26}+R_{m25}+R_{m212}+R_{g27}) \end{cases} \tag{15}$$

Φ_{l21}-Φ_{l29} are the flux of the magnetic leakage circuits. $\Phi_{l21}=F_{m2}/R_{m21}$, $\Phi_{l22}=F_{m2}/(R_{m22}+R_{m123})$, $\Phi_{l23}=2F_{m2}/(R_{m23}+R_{m214})$, $\Phi_{l24}=2F_{m2}/(R_{m26}+R_{m211})$, $\Phi_{l25}=2F_{m2}/(R_{m27}+R_{m210}+R_{m124}+R_{m125})$, $\Phi_{l26}=F_{m2}/R_{m28}$, $\Phi_{l27}=F_{m2}/R_{m29}$, $\Phi_{l28}=F_{m2}/(R_{m215}+R_{m126})$, and $\Phi_{l29}=F_{m2}/R_{m216}$.

According to (11), (12) and (15), the air gap flux expression of topology II is

$$\Phi_{II}=\Phi_{gz1}+\Phi_{gz2}+\Phi_{g16}+\Phi_{g17} \tag{16}$$

The expressions of back electromotive force (EMF) of topologies I and II are

$$e_I=-N_c d(\Phi_{gz1})/dt \tag{17}$$

$$e_{II}=-N_c d(\Phi_{II}-\Phi_{gz2})/dt \tag{18}$$

The expressions of the cogging torque and torque of topologies I and II are [8]

$$T_{cogI} = -(\Phi_{gz1})^2 dR_g(\theta)/d\theta/2 \quad (19)$$

$$T_{cogII} = -(\Phi_{II} - \Phi_{gz2})^2 dR_g(\theta)/d\theta/2 \quad (20)$$

$$T_{eI} = i_{arm}^2 N_c d(\Phi_{gz2}/i_{arm})/d\theta/2 + i_{arm} N_c d(\Phi_{gz1})/d\theta \quad (21)$$

$$T_{eII} = i_{arm}^2 N_c d(\Phi_{gz2}/i_{arm})/d\theta/2 + i_{arm} N_c d(\Phi_{II} - \Phi_{gz2})/d\theta \quad (22)$$

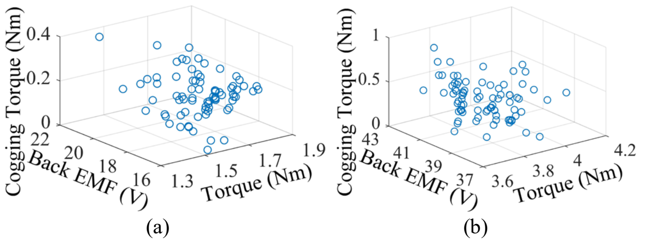

Fig. 10. The results of the EMC method. (a) Topology I. (b) Topology II.

According to (17)–(22), Fig. 10 illustrates the results of cogging torque, back EMF and average torque for topologies I and II based on the EMC method. According to Fig. 10, the ranges of the main parameters can be obtained. In order to further improve the electromagnetic performances of DSPMM, GA is used to obtain the best values of the structural parameters when the average torque and torque ripple are considered as the optimization goals. Fig. 11 describes the Pareto front after topologies I and II are optimized by GA with the same winding turns, the volumes of PM material and machine. To reveal the electromagnetic performance of the presented machine and make a comprehensive comparison, topologies I_a and I_b in [9] are added as topologies III and IV. The specific parameter values of the selected topologies after being optimized by GA are shown in table I.

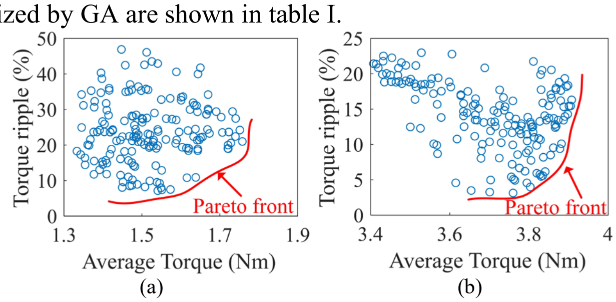

Fig. 11. Pareto front of the optimization. (a) Topology I. (b) Topology II.

TABLE I
MAIN STRUCTURAL PARAMETERS OF TOPOLOGIES

Parameters (mm)	I	II	III	IV	Parameters (mm)	I	II	III	IV
R_{ri}	10.0	10.0	11.2	10.0	W_{sp}	18.0	15.0	16.6	18.0
R_{rr}	19.4	18.2	17.5	19.4	W_{sm}	26.0	26.0	16.6	18.0
R_{ro}	27.0	27.0	27.0	27.0	W_{pm1}	6.5	2.6	3.2	7.2
R_{si}	27.6	27.6	27.6	27.6	W_{pm2}	2.0	2.6	/	/
R_{sy1}	46.4	46.4	46.4	46.4	W_{b1}	4.5	4.5	/	/
R_{sy2}	58.6	58.0	/	/	H_{b1}	1.8	1.8	/	/
R_{so}	69.0	69.0	69.0	58.6	H_{L1}	2.2	2.2	/	/
W_{rp}	11.2	10.4	11.9	11.2	H_{L2}	1.5	1.5	1.5	1.5
L_a	80.0	80.0	80.0	80.0	g	0.6	0.6	0.6	0.6

IV. Experimental Validation

A. Prototype

Fig. 12 shows the prototype and test platform of the proposed DSPMM.

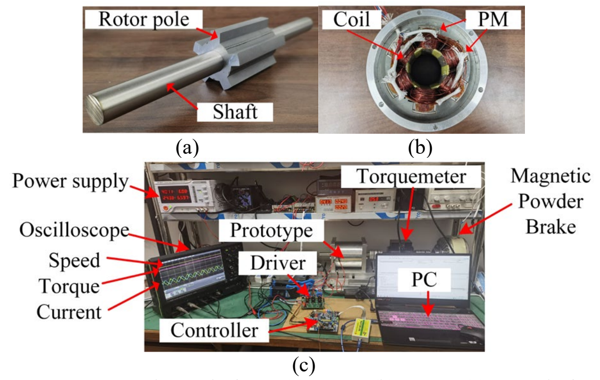

Fig. 12. Prototype and test platform. (a) Rotor. (b) Stator. (c) Test platform.

B. No-load Back EMF and Harmonic Analysis

According to (17) and (18), Fig. 13 displays the back EMFs and harmonics of topologies I, II, III and IV analyzed by FEM and topology II analyzed by EMC and experimental testing. The back EMF amplitudes and total harmonic distortion (THD) of topologies I, II, III and IV analyzed by FEM and topology II analyzed by EMC and test are 18.9V, 44.27V, 36.52V, 14.03V, 47.08V, 43.38V, and 4.89%, 6.56%, 1.82%, 8.03%, 9.02%, 6.34%, respectively.

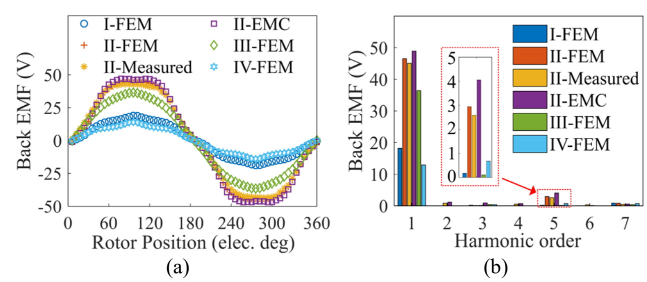

Fig. 13. Back EMFs and harmonics. (a) Back EMF. (b) Harmonic analysis.

C. Cogging Torque and Torque

According to (19)–(22), Fig. 14 illustrates the cogging torque and torque waveforms of topologies I, II, III and IV analyzed by FEM and topology II analyzed by EMC and experimental testing. Their peak values are 0.07 Nm, 0.29 Nm, 0.15 Nm, 0.17 Nm, 0.38 Nm and 0.33 Nm, respectively. Since there is manufacture error, the amplitude of the measurement result of the cogging torque of topology II is higher than that analyzed by FEM. When I_p=7A, their average torques are 1.56 Nm, 3.87 Nm, 3.03 Nm, 1.12 Nm, 4.03 Nm and 3.75 Nm, respectively. The torques of topology II are larger by 148.1%, 27.72% and 245.5% than those of topology I, III and IV, respectively. The torque ripples are 10.51%, 19.21%, 11.57%, 28.14%, 25.42% and 7.87%, respectively. According to Figs. 12 and 13, the back EMF and the average torque of topology I are 34.71% and 39.29% higher than those of topology IV, respectively. The torque ripple and cogging torque of topology I are lower than those of topology IV. Table II shows the comparison results of simulation and experiment.

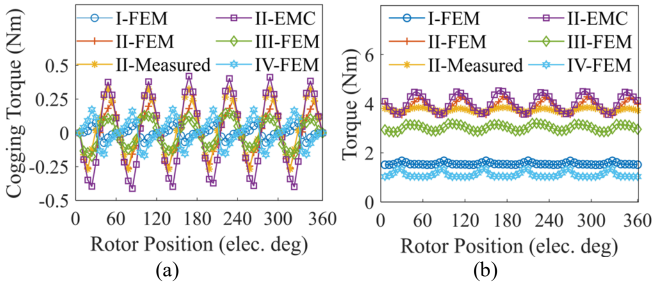

Fig. 14. Cogging torque and torque waveforms of topologies I, II, III and IV analyzed by FEM and topology II analyzed by EMC and experimental testing. (a) Cogging torque. (b) Torque.

TABLE II
COMPARISON RESULTS OF SIMULATION AND EXPERIMENT

Electromagnetic characteristics	Simulation	Experiment
Back EMF (V)	44.27V	43.38V
THD (%)	6.26%	6.34%
Cogging torque (Nm)	0.29Nm	0.33Nm
Torque (Nm)	3.87Nm	3.75Nm
Torque ripple (%)	19.21%	7.87%

V. CONCLUSIONS

In this article, two DSPMMs are developed with AFC, which effectively increases the air gap flux density and torque density. The optimization designs are analyzed by building the EMC models and GA. After the optimization, the back EMF and the average torque of topology I are 34.71% and 39.29% higher than topology IV, respectively. The torque of topology II is larger 148.1%, 27.72% and 245.5% than those of topologies I, III and IV, respectively.

REFERENCES

[1] S. Cai, Z. Q. Zhu, J. C. Mipo, and S. Personnaz, “Investigation of novel doubly salient hybrid excited machine with non-overlapped field winding,” *IEEE Trans. Energy Convers.*, vol. 36, no. 3, pp. 2261–2275, Sep. 2021.

[2] X. Sun, J. Wu, G. Lei, Y. Cai, X. Chen, and Y. Guo, “Torque modeling of a segmented-rotor SRM using maximum-correntropy-criterion-based LSSVR for torque calculation of EVs,” *IEEE J. Emerg. Sel. Topics Power Electron.*, vol. 9, no. 3, pp. 2674–2684, Jun. 2021.

[3] K. Diao, X. Sun, G. Lei, Y. Guo, and J. Zhu, “Multiobjective system level optimization method for switched reluctance motor drive systems using finite-element model,” *IEEE Trans. Ind. Electron.*, vol. 67, no. 12, pp. 10055–10064, Dec. 2020.

[4] H. Cheng, J. Cui, C. Peng, J. Chu, J. Zhou, and Z. Ye, “Electromagnetic characteristics analysis and torque ripple reduction for doubly salient PM machine,” *IEEE Trans. Energy Convers*, vol. 38, no. 3, pp. 1659–1668, Sep. 2023.

[5] X. Sun, K. Diao, G. Lei, Y. Guo, and J. Zhu, “Real-time HIL emulation for a segmented-rotor switched reluctance motor using a new magnetic equivalent circuit,” *IEEE Trans. Power Electron.*, vol. 35, no. 4, pp. 3841–3849, Apr. 2020.

[6] X. Sun, B. Wan, G. Lei, X. Tian, Y. Guo, and J. Zhu, “Multiobjective and multiphysics design optimization of a switched reluctance motor for electric vehicle applications,” *IEEE Trans. Energy Convers.*, vol. 36, no. 4, pp. 3294–3304, Dec. 2021.

[7] Y. Du, C. Zhang, X. Zhu, F. Xiao, Y. Sun, Y. Zuo, and L. Quan, “Principle and analysis of doubly salient PM motor with π-shaped stator iron core segments,” *IEEE Trans. Ind. Electron.*, vol. 66, no. 3, pp. 1962–1972, Mar. 2019.

[8] M. Cheng, K. T. Chau, C. C. Chan, E. Zhou, and X. Huang, “Nonlinear varying-network magnetic circuit analysis for doubly salient permanent-magnet motors,” *IEEE Trans. Magn.*, vol. 36, no. 1, pp. 339–348, Jan. 2000.

[9] K. Guo, C. Liu, C. Li, and Y. Guo, “Comparison analysis of doubly salient permanent magnet machine,” *Proc. 2023 IEEE Int. Conf. on Applied Superconductivity and Electromagnetic Devices* (*ASEMD*), Tianjin, China, Oct. 27-29, 2023.